

Inverse imaging using total field measurements

Chandan Bhat and Uday K. Khankhoje, *Senior Member, IEEE*

Abstract—Most microwave inverse imaging algorithms rely on measurements of both, the total and the incident electric field, in order to estimate the dielectric properties of an unknown scattering object. We propose a new technique to jointly estimate the incident field and relative permittivity of a heterogeneous dielectric object from measurements of the total electric field alone. For the first task, we express the incident field as a collection of plane waves, and estimate the wave coefficients from the given data by leveraging sparsity of the plane wave spectrum and obtain the solution via a constrained re-weighted L_1 norm minimization technique. Subsequently, we estimate the permittivity and geometry of the scattering object using a two-fold subspace optimization method. We evaluate the performance of our algorithm on synthetically generated object, as well as experimental data. For synthetic objects, the accuracy in reconstruction of the incident field and relative permittivity is $\approx 93\%$ for field measurements with 15 dB signal to noise ratio, while the accuracy obtained for an experimental data set was $\approx 90\%$.

Index Terms—Microwave imaging, Compressive Sensing, inverse scattering

I. INTRODUCTION

Microwave inverse imaging concerns itself with the reconstruction of the relative permittivity of a remote scattering object (SO) in a given domain of interest \mathcal{D} . Inverse imaging algorithms, such as the Born type approximation methods [1], contrast source inversion (CSI) [2], and subspace optimization methods (SOM) [3] require knowledge of the scattered field information on a measurement contour \mathcal{C} , which in turn requires complete knowledge of the incident field in \mathcal{D} . Incident fields are field-measurements made in the absence of the scattering object. In most practical scenarios, the total and incident fields are measured separately (see [4] for e.g.). However, incident field information is not readily available in many real world settings, particularly when the SO is spatially fixed and cannot be removed, for e.g. in the case of buried object detection using ground penetrating radar. In such cases reconstruction of the relative permittivity of the SO should be achieved with only total field data. An intermediate step in such a problem involves the retrieval of incident fields, which is accomplished via the solution of an optimization problem.

Related work: In [5] the incident field inside \mathcal{D} is estimated using a source reconstruction method where equivalent currents are estimated on a surface which encloses the transmitters. This approach does not completely eliminate the need for the incident field, as the estimation inside \mathcal{D} is achieved by incident field measurements on \mathcal{C} . In [6] the incident field is estimated using the surface equivalence principle by measuring the tangential components of *both* total electric

C. Bhat (e-mail: chandanbhat21@gmail.com) and U. K. Khankhoje (corresponding author, e-mail: uday@ee.iitm.ac.in) are with the Department of Electrical Engineering, Indian Institute of Technology Madras, Chennai, India.

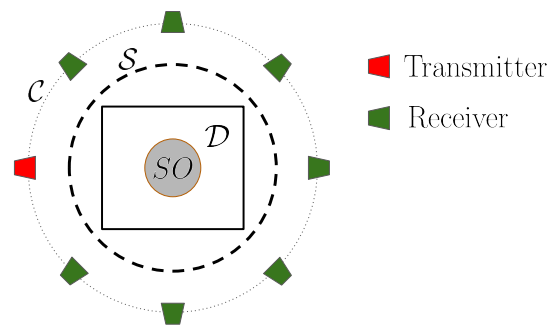


Fig. 1: Schematic of the imaging experiment where the transmitters and receivers are placed a contour \mathcal{C} . A scattering object SO with unknown permittivity is within a domain of interest \mathcal{D} , immersed in freespace. S denotes a Huygens' surface that encloses \mathcal{D} .

and magnetic fields; subsequently, the estimated incident field is used to retrieve the scatterer permittivity in [7]. In [8] the incident field data is recovered from total electric and magnetic field measurements by representing the incident field as a summation of Bessel functions. A disadvantage of these methods are that they require both total electric and magnetic field measurements.

Our contributions: We consider a two-dimensional, transverse-magnetic polarization scenario and propose a surface integral formulation that estimates the incident field on \mathcal{C} and inside \mathcal{D} using only the total electric field measurements on \mathcal{C} . We do so by expressing the unknown incident field in terms of a plane wave expansion, and then casting the problem in a constrained optimization framework that employs a novel re-weighted L_1 norm minimization strategy. The use of the L_1 norm leverages the implicit sparsity in the plane wave spectrum, while the constraints make sure that the measured data is consistent with the estimated incident fields. Subsequently, we reconstruct the relative permittivity profile of the SO in \mathcal{D} using a two-fold subspace optimization method (TSOM) [9]. The advantage of the proposed method is that it completely eliminates the need for information of the incident electric field, and only relies on total electric field measurements. We validate our method by estimating the incident field and reconstructing the SO in two scenarios:

- (1) a synthetically generated case (where we also consider the role of the measurements being corrupted by noise), and
- (2) using an experimental “Fresnel” data set [4] which includes measurements of total and incident electric fields on \mathcal{C} .

II. PROBLEM FORMULATION – FOUNDING EQUATIONS

In this section we outline the basic mathematical tools used for the incident field reconstruction and inverse imaging.

1) *Incident field estimation – surface integral equations:*

As per Huygens' principle, the field outside any contour \mathcal{S} can be expressed as a sum of primary sources (i.e. incident fields) and secondary sources (i.e. equivalent tangential electric and magnetic currents on \mathcal{S}); the Extinction theorem in turn gives us consistency relations between the incident field and the equivalent tangential electric and magnetic currents [10]. The incident field is approximated as a linear combination of N_i planewaves travelling in different directions [11], i.e. :

$$E^i(\vec{r}) = \sum_{i=1}^{N_i} c_i \exp(-jk_i \cdot \vec{r}), \quad (1)$$

where $\vec{k}_i = k_0[\cos\theta_i, \sin\theta_i]^T$, k_0 is the free space wave number, θ_i 's are the wavevector angles, and c_i 's are complex wave coefficients; the number N_i is pre-assigned and much larger than the actual number of planewaves. Thus, by considering the founding relations mentioned above (and detailed below), we can arrive at a system of equations relating the measurements to the unknowns to be determined.

Huygens's principle: The total field at any location \vec{r} outside the Huygens' surface \mathcal{S} (see Fig. 1) is expressed as [10]:

$$E^t(\vec{r}) = E^i(\vec{r}) - \oint_{\mathcal{S}} [G(\vec{r}, \vec{r}') \nabla' E_S^t(\vec{r}') - \nabla' G(\vec{r}, \vec{r}') E_S^t(\vec{r}')] \cdot \hat{n}_{\mathcal{S}} dl', \quad \vec{r} \in \mathcal{C}, \quad (2)$$

where E_S^t is the tangential electric field on \mathcal{S} , $\nabla E_S^t \cdot \hat{n}_{\mathcal{S}}$ is proportional to the tangential magnetic field on \mathcal{S} , $G(\vec{r}, \vec{r}')$ is the 2D free space Green's function, $\hat{n}_{\mathcal{S}}$ is the outward normal to the surface \mathcal{S} , and ∇' refers to the gradient with respect to primed coordinates, \vec{r}' .

Extinction theorem: The consistency relation between the electric and magnetic fields on \mathcal{S} are given as [12]:

$$E^i(\vec{r}) - \oint_{\mathcal{S}} [G(\vec{r}, \vec{r}') \nabla' E_S^t(\vec{r}') - \nabla' G(\vec{r}, \vec{r}') E_S^t(\vec{r}')] \cdot \hat{n}_{\mathcal{S}} dl' = 0, \quad \vec{r} \in \mathcal{S} \quad (3)$$

For numerical estimation, we discretize the surface \mathcal{S} into N segments, and expand the tangential electric and magnetic fields in the pulse basis function (see [13, Sec. 3]). This gives us the discretized version of the Huygens' principle (i.e. Eq. (2) with Eq. (1)) as:

$$A_D x = b + \nu, \quad (4)$$

where $A_D \in \mathbb{C}^{M \times (2N+N_i)}$ is called as *data* matrix, the unknown vector is denoted as $x \in \mathbb{C}^{(2N+N_i) \times 1}$, with the first $2N$ terms corresponding to the tangential electric and magnetic fields and the next N_i terms are the coefficients of incident field expansion (i.e. c_i 's). The vector $b = [E^t(\vec{r}_1) \cdots E^t(\vec{r}_M)]^T$ contains M measurements of the total electric field, and $\nu \in \mathbb{C}^M$ represents measurement noise (modelled as complex additive white Gaussian noise for synthetic measurements). The discretized version of the extinction theorem (i.e. Eq. (3) with Eq. (1)) is:

$$A_S x = \vec{0} \quad (5)$$

where $A_S \in \mathbb{C}^{N \times (2N+N_i)}$ is called as *state* matrix, $\vec{0} \in \mathbb{R}^N$. The elements of the matrix A_D and A_S are computed as

per standard relations (see [14, Eq. 7]). The Eqs. (4) and (5) are referred to in the literature as *data* and *state* equations respectively.

2) *Inverse imaging formulation – volume integral equations:* Consider the figure schematic as per Fig. 1. The relation between the fields and scatterer permittivity is given by the Fredholm integral equation of the second kind [1]:

$$E^t(\vec{r}) = E^i(\vec{r}) + k_0^2 \int_{\mathcal{D}} G(\vec{r}, \vec{r}') E^t(\vec{r}') \chi(\vec{r}') d\vec{r}', \quad (6)$$

where $E^t(\vec{r})$, $E^i(\vec{r})$ are the total and incident field, respectively, and $\chi(\vec{r}) = \epsilon_r(\vec{r}) - 1$ is referred to as the dielectric contrast given relative permittivity $\epsilon_r(\vec{r})$.

A total of M receivers, which measure the total field E^t , are placed on \mathcal{C} . Total field measurements are recorded for N_I illuminations. By defining a convenient "contrast source" term, $w(\vec{r}) = E^t(\vec{r})\chi(\vec{r})$ for $\vec{r} \in \mathcal{D}$, and discretizing \mathcal{D} on a square grid of size $L \times L$, we arrive at the following equations for the p^{th} illumination [2]:

$$w_p = X(e_p + G_D w_p), \quad \vec{r} \in \mathcal{D} \quad (7)$$

$$d_p = E_p^i + G_S w_p, \quad \vec{r} \in \mathcal{C} \quad (8)$$

where $\{w_p, e_p, E_p^i, d_p\} \in \mathbb{C}^{L^2}$ are discretized versions of the contrast source, incident field in \mathcal{D} and \mathcal{C} (obtained by substituting the estimated coefficients c_i in Eq. (1), and \vec{r} as per Eqns. (7),(8)) and total fields, respectively; $X \in \mathbb{C}^{L^2 \times L^2}$ is a diagonal matrix of contrasts of each grid. The matrices $G_D \in \mathbb{C}^{L^2 \times L^2}$ and $G_S \in \mathbb{C}^{M \times L^2}$ are discretized versions of $G(\vec{r}, \vec{r}')$; G_D is obtained from Eq. (6) when $\vec{r} \in \mathcal{D}$, and G_S is obtained from Eq. (6) when $\vec{r} \in \mathcal{C}$.

Summary: In total field inverse imaging, the aim is to reconstruct the contrast $\chi(\vec{r})$, $\vec{r} \in \mathcal{D}$ with only total electric field measurements. Eqs. (4),(5) are the governing equations for incident field estimation, whereas Eqs. (7),(8) are the governing equations for subsequent permittivity estimation.

III. SOLVING THE INVERSE PROBLEMS

This section provides the details of the solution strategies and algorithms employed in incident field estimation and further reconstruction of relative permittivity of the SO .

1) *Stage I: incident field estimation:* In our recent work [14] we developed the Total field – Compressive Sensing based Subspace Optimization Method (TCS-SOM) to estimate x from total field measurements. The solution, x , is decomposed into two orthogonal vector subspaces, called the major (x^+) and minor (x^-) components, respectively (i.e. $x = x^+ + x^-$). The singular value spectrum of the data matrix, A_D , is used to partition the solution between these two subspaces. The major part, x^+ , is uniquely determined from the *data* equation (Eq. 4) by using a truncated singular value decomposition (SVD) [14, Eq. 13], i.e. $x^+ = \sum_{i=1}^{L_0} u_i^H b v_i / \sigma_i$, where u_i, v_i are the left and right singular vectors of A_D , respectively, σ_i represent the singular values, and L_0 is a parameter estimated using Morozov's principle (see [14, Eq. 14]).

In contrast, the minor space component of the solution, x^- , is not determined from the measurements, and its estimation is based on the following two observations: (i) we consider

a sufficiently large N_i for the incident field expansion which suggests that only a few of the coefficients c'_i s are significant [11], and (ii) the tangential fields are known to be sparse in certain transformed domains (e.g. in the discrete Fourier or Cosine transformed-domain [15]). These observations of sparsity motivate determining x^- using Compressive Sensing techniques [13], [16]. Thus, having obtained the major part x^+ in the first step, the objective function for estimating the minor part x^- is formulated using the re-weighted L_1 minimization method [17] is given by:

$$\begin{aligned} & \underset{x^-}{\text{minimize}} && \|W\{\mathcal{M}I_1(x^+ + x^-) + I_2(x^+ + x^-)\}\|_1 \\ & \text{subject to} && \|A_D(x^+ + x^-) - (b + \nu)\|_2 \leq \epsilon, \\ & && \|A_S(x^+ + x^-)\|_2 \leq \eta \end{aligned} \quad (9)$$

where, W is a diagonal re-weighting matrix, \mathcal{M} is a transformation matrix (for e.g. the DFT or DCT basis); also see [14, Eq. 15]. $I_1 \in \mathbb{R}^{2N \times (2N+N_i)}$ and $I_2 \in \mathbb{R}^{N_i \times (2N+N_i)}$ are block diagonal matrices which when multiplied to the vector x extract the coefficients corresponding to tangential and incident fields, respectively (thus facilitating their transformation by \mathcal{M}), ϵ is the noise variance and η is an estimate of the discretization error in the State equation.

2) *Stage II: Inverse scattering solution:* Among the various methods to solve the inverse scattering problem (i.e. of estimating dielectric contrast given field data), we choose the two-fold SOM (TSOM) [9] with an additional total variation (TV) regularization for the contrast (see [18, Eq. 5] specialized to a single frequency for formulations details).

IV. RESULTS - SYNTHETIC AND EXPERIMENTAL DATA

In this section, we evaluate the accuracy of our proposed algorithm via numerical examples. We visualize the reconstruction of the scatterer for: (a) synthetic data – where the measurements are corrupted by two noise levels with signal to noise ratio (SNR) of 25 dB and 15 dB, and (b) experimental data (Fresnel database [4]). The results are programmed in MATLAB 2019b on a 2.4GHz Quad-Core Intel i5 processor, using 8GB RAM.

Synthetic data : We choose a 2D cylinder and the ‘Austria’ profile [19] to test the algorithm’s performance of recovering the incident field and for inverse imaging. The simulation domain, \mathcal{D} , is 1×1 m for 2D cylindrical object and 2×2 m for the ‘Austria’ profile. We consider a 16 transmitters \times 64 receivers configuration, where the transmitters emit an incident field composed of seven plane waves. The receivers are placed on a contour (\mathcal{C}) of radius 4 m which measures only the total electric field. We vary the relative permittivity of the scatterer from 1.4 to 2.6 and radius of the cylinder from 0.2 m to 0.6 m with a 400 MHz operating frequency. For the inverse solver (see Eq. 7) \mathcal{D} is discretized into a 32×32 grid. The total electric field data is generated using the volume integral (VI) method which is validated with the Mie series solution [20] for scattering from a 2D dielectric cylinder of radius 1 m.

1) *Incident field estimation:* The Huygens’ surface \mathcal{S} (which encloses \mathcal{D}) is discretized at $\lambda/10$. The number of coefficients in the expansion of the incident field is $N_i = 100$,

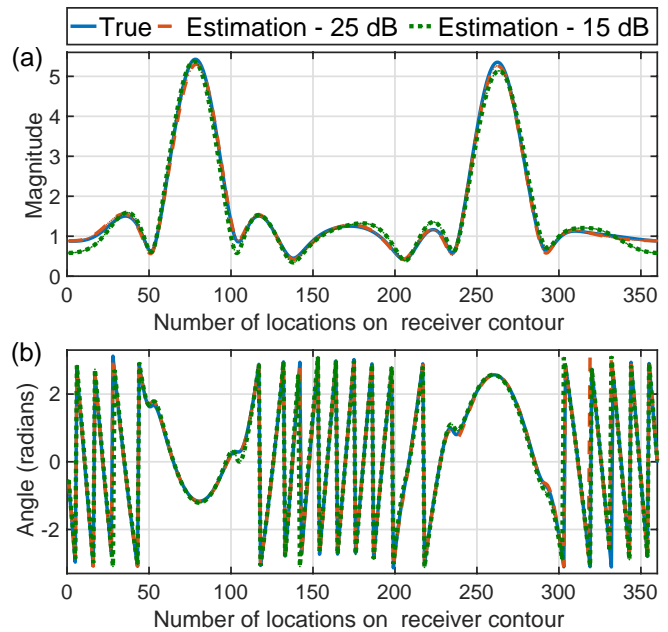


Fig. 2: Comparison of (a) magnitude (V/m), (b) phase of true and estimated incident fields on the receiver contour \mathcal{C} for 360 locations. The true field (for one transmitter) consists of planewaves travelling at these angles (in degrees): $[-10, -\frac{20}{3}, -\frac{10}{3}, 0, \frac{10}{3}, \frac{20}{3}, 10]$, with these coefficients: $[0.58 + 0.42j, 0.14 + 0.77j, 0.74 + 0.49j, 0.58 + 0.43j, 0.77 + 0.50j, 0.38 + 0.48j, 0.97 + 0.40j]$. The accuracy of estimation of incident field is 98.6% and 94.2% for total field measurements with 25 dB and 15 dB SNR. In the former case, the reconstructed planewave angles are: $[-11.06, -7.72, -3.48, 0.45, 5.00, 9.85, 15.00]$, and the coefficients are: $[0.35 + 0.16j, 0.43 + 0.87j, 0.61 + 0.65i, 0.96 + 0.50i, 0.80 + 0.76i, 1.06 + 0.52i, 0.02 - 0.02i]$.

which makes the total number of unknowns $N_t = 2N + 100$. For a 2D cylindrical scatterer with radius 0.4 m, $N_t = 2 \times 56 + 100 = 212$. We solve the optimization problem (Eq. 9) using reweighted L_1 minimization [17] for each illumination from the transmitter. The time taken for the incident field estimation for all the illuminations is 560s. Fig. 2 and 3 shows the comparison of true and estimated incident field on \mathcal{C} and \mathcal{D} respectively, for a single illumination. We define the relative incident field error as

$$err_i = \frac{\|E^i(\vec{r}) - \hat{E}^i(\vec{r})\|_2}{\|E^i(\vec{r})\|_2} \quad (10)$$

where $\hat{E}^i(r)$ is the estimated incident field. The average error in estimation of incident field for all the 16 illuminations are 3.7% on \mathcal{C} and 3.9% on \mathcal{D} for 25 dB SNR and 7.9% and 8.3% for 15 dB SNR respectively. We note that since the data matrix need not satisfy the restricted isometry property required for a unique solution to the compressive sensing problem [16], the reconstructed coefficients of the incident field are not exact; however, the reconstructed field over a chosen contour or the entire domain matches the true field to high accuracy.

2) *Inverse Imaging:* The incident field information on \mathcal{C} and \mathcal{D} which are obtained from the previous stage is used in

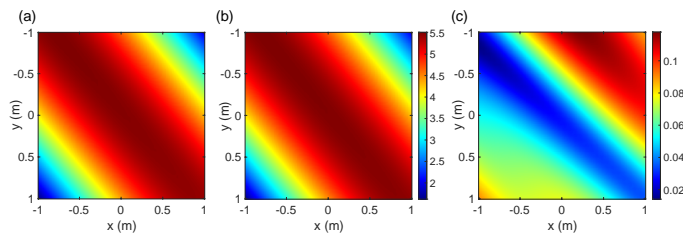


Fig. 3: (a) True, (b) estimated incident field magnitude (V/m, with common scale bar) over the entire domain of interest (\mathcal{D}), and (c) absolute difference between true and estimated incident fields. Measurements ($M = 64$) have 25 dB SNR, and field estimation accuracy is 97.2%.

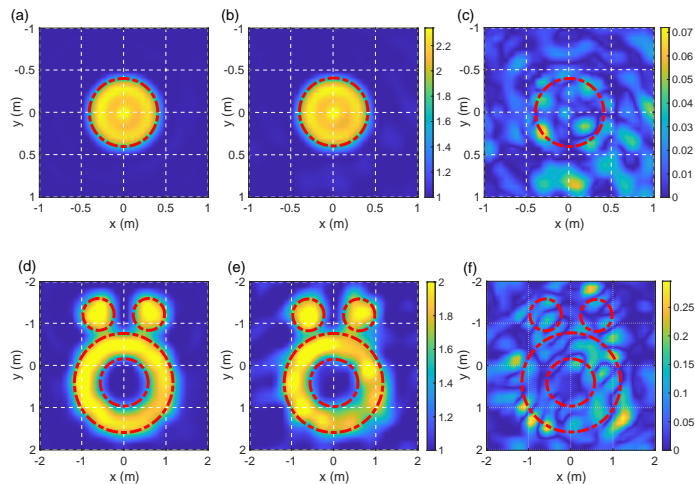


Fig. 4: Reconstructed permittivity profile of (top) a 2D cylindrical scattering object (true relative permittivity: 2.2, radius: 0.4m) and (bottom) the Austria profile (true relative permittivity is 2) with illuminations (a),(d) known (TE \approx 3% and 8%, IE \approx 5% and 10%); (b),(e) estimated from total field measurements (TE \approx 3.5% and 10%, IE \approx 5.5% and 12%); (c) absolute difference of (a) and (b); and (f) absolute difference between (d) and (e). Measurements ($M = 64$) have 25 dB SNR; dotted red contours indicate the true shape of the scatterers.

inverse imaging algorithms. Fig. 4 shows the reconstruction of a 2D cylindrical scatterer, and the Austria profile. To measure the accuracy of the inverse imaging algorithm we define two error quantities (a) total error (TE) and (b) internal error (IE):

$$\text{TE} = \frac{1}{|\mathcal{D}|} \sum_{i \in \mathcal{D}} \frac{|\epsilon_r(i) - \hat{\epsilon}_r(i)|}{|\epsilon_r(i)|}, \quad \text{IE} = \frac{1}{|SO|} \sum_{i \in SO} \frac{|\epsilon_r(i) - \hat{\epsilon}_r(i)|}{|\epsilon_r(i)|} \quad (11)$$

where $\epsilon_r(\cdot)$, $\hat{\epsilon}_r(\cdot)$ are the true and estimated relativity permittivity, and $|P|$ denotes the size of set P .

The inverse scattering problem is highly nonlinear with respect to the size and permittivity of the SO . Therefore, for a fixed frequency of operation, the algorithm fails to reconstruct larger and higher permittivity scatterers (we have shown a deep learning-based technique to overcome this limitation in earlier work [19]). Fig. 5 shows the internal and total errors in reconstruction of the cylindrical scatterer for varying radius

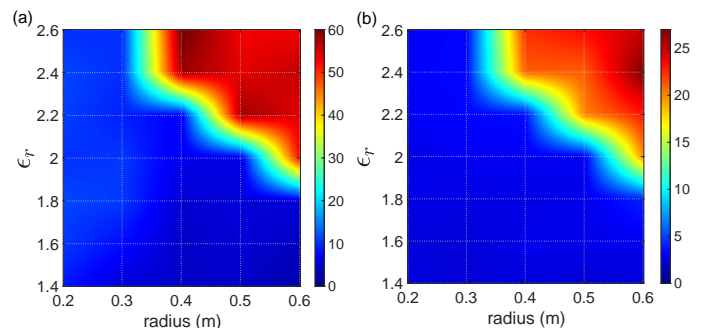


Fig. 5: Percentage (a) internal error (IE) and (b) total error (TE) for 2D cylindrical scattering object of varying radius and permittivity when the illuminations are estimated. The frequency of operation is 400 MHz.

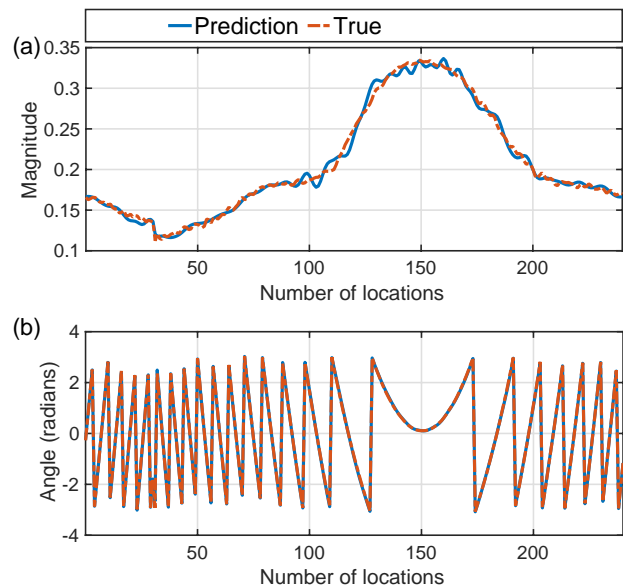


Fig. 6: Reconstruction of (a) magnitude (V/m), and (b) phase of incident field from total field measurements for Fresnel data set at 2 GHz. The error in incident field estimation is 3.1%.

and permittivity. We also investigated the reconstruction errors in the more conventional case where the incident illuminations are known, and found that our method performs only marginally worse (approximately 1% more error) when the illuminations are estimated.

3) *Experimental data*: We evaluate our method with the experimental data obtained from Fresnel database [4]. We consider an in-homogeneous object *FoamDieIntTM* at frequency 2 GHz. Fig. 7(a) shows the relative permittivity profile of the scatterer. The dataset consists of the total and incident field at 241 receiver locations from 8 transmitters. The receivers are placed with a gap of 1 degree. For the inverse solver, we consider only 80 total field measurements from the dataset. We assume the noise variance (ϵ) to be known for the synthetic data simulations, while we set it as $\epsilon = 0.001 \|b\|_2$ for experimental data. The discretization error in the State equation η is empirically set to 0.01.

Fig. 6 shows the comparison of the experimentally measured

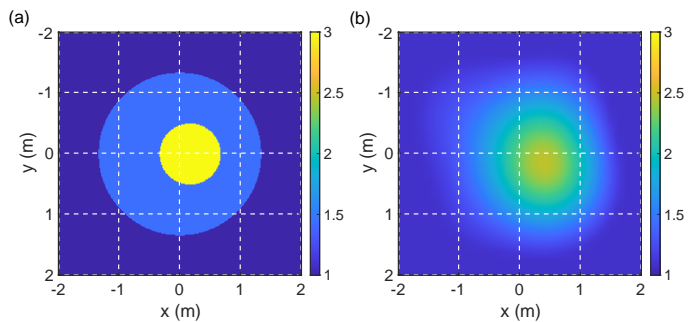


Fig. 7: (a) True and (b) estimated relative permittivity of an inhomogeneous scatterer: A plastic cylinder (radius 15 mm) of relative permittivity 3 ± 0.3 embedded inside a foam cylinder (radius 40 mm) of relative permittivity of 1.45 ± 0.15 .

incident field and the estimated incident field on all 241 receiver locations for a single illumination. The average error in incident field estimation is 6.6%.

An important consideration is the comparison between the cases where the incident field information is either available or not. In our extensive numerical studies, we find that the accuracy degrades by a very small amount ($\approx 1 - 2\%$) if this information is not available and is instead estimated by the techniques shown in this Letter.

V. CONCLUSION

In this Letter, we have shown a promising technique for solving the microwave imaging problem from measurements of the total electric field measurements alone and without any information of the incident field; the latter was estimated as an intermediate step. The use of the Extinction theorem helped us to eliminate the need for *both* electric and magnetic field measurements. We evaluated the proposed method for synthetic data with varying object permittivity and size. Furthermore, we have also validated the total field inverse imaging for an experimental dataset. For synthetic data we estimate the permittivity with noisy total field measurements. For all the SNRs considered in the synthetic experiments, the accuracy of inverse imaging was found to always be in excess of 93 % (both total and internal error metrics). For experimental data the total and internal reconstruction accuracy was 91% and 85%, respectively. An extension of these techniques to three dimensional settings is in progress.

REFERENCES

- [1] Y. Wang and W. C. Chew, "An iterative solution of the two-dimensional electromagnetic inverse scattering problem," *International Journal of Imaging Systems and Technology*, vol. 1, no. 1, pp. 100–108, 1989.
- [2] P. M. Van Den Berg and R. E. Kleinman, "A contrast source inversion method," *Inverse problems*, vol. 13, no. 6, p. 1607, 1997.
- [3] X. Chen, "Subspace-based optimization method for solving inverse-scattering problems," *IEEE Transactions on Geoscience and Remote Sensing*, vol. 48, no. 1, pp. 42–49, 2009.
- [4] J.-M. Geffrin, P. Sabouroux, and C. Eyraud, "Free space experimental scattering database continuation: experimental set-up and measurement precision," *inverse Problems*, vol. 21, no. 6, p. S117, 2005.
- [5] C. Narendra, I. Jeffrey, and P. Mojabi, "Using the source reconstruction method to model incident fields in microwave tomography," *IEEE Antennas and Wireless Propagation Letters*, vol. 16, pp. 46–49, 2016.

- [6] R. Yang, Z. Meng, and T. Takenaka, "Extraction of incident field from total field data," in *2016 Progress in Electromagnetic Research Symposium (PIERS)*. IEEE, 2016, pp. 4073–4077.
- [7] R. Yang, Z. Meng, and T. Takenaka, "Conjugate gradient method applied to inverse scattering with no prior information on incident field," in *2017 Progress in Electromagnetics Research Symposium-Fall (PIERS-FALL)*. IEEE, 2017, pp. 731–736.
- [8] T. Tsuburaya, Z. Meng, and T. Takenaka, "Inverse scattering analysis from measurement data of total electric and magnetic fields by means of cylindrical-wave expansion," *Electronics*, vol. 8, no. 4, p. 417, 2019.
- [9] Y. Zhong and X. Chen, "Twofold subspace-based optimization method for solving inverse scattering problems," *Inverse Problems*, vol. 25, no. 8, p. 085003, 2009.
- [10] W. C. Chew, "Waves and fields in inhomogeneous media (electromagnetic waves)," 1995.
- [11] A. C. Austin and M. J. Neve, "Efficient field reconstruction using compressive sensing," *IEEE Transactions on Antennas and Propagation*, vol. 66, no. 3, pp. 1624–1627, 2018.
- [12] L. Tsang and J. A. Kong, *Scattering of electromagnetic waves: advanced topics*. John Wiley & Sons, 2004, vol. 26.
- [13] C. Bhat, K. Sastry, and U. K. Khankhoje, "Compressive sensing approaches for the prediction of scattered electromagnetic fields," *JOSA A*, vol. 37, no. 7, pp. 1166–1174, 2020.
- [14] K. Sastry, C. Bhat, R. Solimene, and U. K. Khankhoje, "Electromagnetic field imaging in arbitrary scattering environments," *IEEE Transactions on Computational Imaging*, vol. 7, pp. 224–233, 2021.
- [15] X. Chen, *Computational methods for electromagnetic inverse scattering*. John Wiley & Sons, 2018.
- [16] E. J. Candès and M. B. Wakin, "An introduction to compressive sampling [a sensing/sampling paradigm that goes against the common knowledge in data acquisition]," *IEEE signal processing magazine*, vol. 25, no. 2, pp. 21–30, 2008.
- [17] E. J. Candès, M. B. Wakin, and S. P. Boyd, "Enhancing sparsity by reweighted l_1 minimization," *Journal of Fourier analysis and applications*, vol. 14, no. 5, pp. 877–905, 2008.
- [18] Y. Kalepu, Y. Sanghvi, and U. K. Khankhoje, "Reconstructing dispersive scatterers with minimal frequency data," *IEEE Geoscience and Remote Sensing Letters*, vol. 18, no. 1, pp. 62–66, 2020.
- [19] Y. Sanghvi, Y. Kalepu, and U. K. Khankhoje, "Embedding deep learning in inverse scattering problems," *IEEE Transactions on Computational Imaging*, vol. 6, pp. 46–56, 2019.
- [20] C. A. Balanis, *Advanced engineering electromagnetics*. John Wiley & Sons, 2012.